Analytical and Experimental Study of a Metamaterial Beam with Grading Piezoelectric Transducers for Vibration Attenuation Band Widening

Yupei Jian[1], Guobiao Hu[2], Lihua Tang[1]*, Wei Tang[3], Moein Abdi[1], Kean C Aw[1]

[1] Department of Mechanical and Mechatronics Engineering, The University of Auckland, Auckland 1010, New Zealand

[2] School of Civil and Environmental Engineering, Nanyang Technological University, Singapore 639798, Singapore

[3] School of Automation, Northwestern Polytechnical University, Xi'an 710072, P.R. China

* corresponding author: l.tang@auckland.ac.nz

Abstract

This paper analytically and experimentally investigates the potential of a piezoelectric metamaterial beam with a spatial grading pattern for broadband vibration attenuation. Distributed bimorph piezoelectrics with varying lengths form the "graded" manner. A fully coupled analytical model based on the transfer matrix function is developed to exhibit the vibration attenuation capabilities. The band structure of the graded supercell structure and the transmittance response of the finite-length counterpart show that the bandwidth of the vibration attenuation zone can be significantly broadened by the spatial variation of the piezoelectric transducers, while multiple resonant-related passbands/peaks occur. By properly introducing electrical damping (e.g., 200 Ω), the resonant peaks can be significantly attenuated. Subsequently, for the first time, we experimentally confirmed the broadband vibration attenuation performance of the graded piezoelectric metamaterial. The harmonic excitation test demonstrates that the enlarged attenuation region can be achieved: with the spatial variation of 1 millimetre, the attenuation bandwidth can be increased up to 80% as compared to conventional metamaterial with identical piezoelectric patches. Furthermore, the white noise excitation test verifies the broadband attenuation capabilities. The results show that the root-mean-square (RMS) acceleration of the graded metamaterial beam is remarkably reduced as compared to that of the conventional one.

Keywords: Metamaterial; Bandgap; Grading piezoelectric transducers; Broadband vibration attenuation.

1. Introduction

The engineered composite structure containing periodic arrays of local resonators, or a popular term, locally resonant (LR) metamaterials, are regarded as one of the state-of-the-art technologies used to manipulate waves through bandgaps. One main motivation for developing this type of artificial structures derives from the increasing demand for vibration mitigation in the modern aerospace, automotive and transportation industries. The miniature, lightweight, and high-precision devices used intensively in these fields are more susceptible to damage from environmental vibrations [1], requiring new vibration suppression approaches. In this context, LR metamaterial, which can attenuate sub-wavelength waves, has unscreened new routes for low-frequency vibration control in a relatively small structure [2].

To make the metamaterial adaptive to different working conditions, researchers have reported various metamaterial-based structures with reconfigurable or adjustable abilities, including magnetorheological elastomer isolator-based metamaterials [3, 4], bistable/multistable metamaterials [5-7], thermally tuning-based metamaterials [8-10], and origami type metamaterials [11-13], to name a few. Among them, piezoelectric metamaterial implemented by integrating shunted piezoelectric elements into structures has received wide attention. Analogously to mechanical oscillators, the antiresonance induced by the resonant shunts can open the LR bandgap, which can be tuned by modifying the circuitry configuration. In contrast to some mechanical metamaterials whose vibration attenuation ability depends on the ratio of the added-on mass to the host structure [14], the vibration energy in the piezoelectric metamaterial is dissipated by shunt circuits and therefore avoids the significant additional mass [15].

The crucial parts of the piezoelectric metamaterial, i.e., the shunt resonant circuits, are usually implemented by analogy electronic components. To overcome the limitation in terms of physical size and impedance value of passive components such as inductors, operational amplifier-based synthetic circuits are widely adopted to emulate the behavior of real inductance [16, 17]. Furthermore, owing to the well-established control techniques, digital resonant circuits that combine analogy circuits and microcontrollers, show the potential for designing programmable shunt circuits [18, 19]. Transfer functions written in the microcontroller units determine the relationship of the current and voltage of the piezoelectric transducer and form an equivalent electrical impedance [20]. In addition, the piezoelectric metamaterial's vibration mitigation property highly relies on the electromechanical coupling effect [21], and the bandgap induced by simple resonant shunts is normally narrow. To this end, advanced shunt circuits are proposed to broaden the bandgap width and enhance the bandgap attenuation intensity, including negative capacitance circuits [22, 23], nonlinear shunt circuits [24, 25], switching shunt circuits [26, 27], and adaptive shunt circuits [28].

The aforementioned studies mainly considered local resonators with periodic geometric and dynamic properties. More recently, with a special focus on bandgap widening and wave manipulation, metamaterials with a certain degree of aperiodicity have become a topic of interest. The design guidelines can basically be classified into disordered design and graded design, both of which provide an additional tolerance for manufacturing. Concerning the first design, Fabro et al. [29] investigated the wave propagation in the beam-type metamaterial with randomly varying properties and concluded that the uncertainties in the system might either contribute to the enhancement of bandgap, or prevent its formation. Pan et al. [30] evaluated the uncertainties in a piezoelectric metamaterial, showing that the bandgap behavior is sensitive to circuitry parameter uncertainty. Additionally, instead of random disorder, researchers were dedicated to employing optimization algorithms to handle the arbitrary system parameters to seek optimal vibration attenuation performance [31-33]. The Anderson localization phenomenon was also observed in the disordered metamaterial systems [34, 35], showing potential in signal filtering [36] and waveguiding applications [37]. Regarding the graded design (i.e., geometric/material properties of the periodic unit cell are gradually vary based on deterministic functions), Hu et al. [38] used a fixed value to constrain the frequency spacing of the natural frequencies of the mass-spring type resonators, aiming at broadening the attenuation zones. With the same concept, Alshaqaq et al. [39] proposed a piezoelectric metamaterial shunted to resonant circuits with grading circuity configuration. In that study, except for a wider attenuation zone, a rainbow trapping phenomenon occurs, which benefited broadband energy harvesting since the vibrational energy related to different frequency wave components was separately localized to different positions. Later on, the idea of grading circuity parameters was applied to negative capacitance shunts to further enlarge the attenuation zone [40]. Recently, instead of grading circuit parameters, we investigated a graded metamaterial with spatially varying electrodes [41]. Gradually changing the electrical properties of the piezoelectric cells seperated by electrodes brings the potential to expand the attenuation zone. However, there are still some gaps in the field of graded piezoelectric metamaterials. First, previous studies have demonstrated the broadband attenuation properties of graded metamaterials via the transmittances of finite length models, but few have studied their bandgap behaviors in band structures. Second, the research was still at the conceptual stage. In particular, the sandwich structure based on a full-coverage piezoelectric transducer in [39, 41] makes the experimental validation challenging due to the following difficulties: (1) ensuring insulation of adjacent units is not easy, and (2) a single piezoelectric patch cannot be fabricated too long to avoid high fragility.

In this work, we continue to explore the idea of varying piezoelectric transducers in our previous study [41]. Unlike the idealized model in [41], we consider a more practical one, i.e., a metamaterial beam partially covered by piezoelectric transducers and configured in a grading pattern. This configuration makes experimental validation possible. Moreover, in addition to the transmittance analysis for finitely-long structures presented in [41], a graded supercell analysis based on the transfer matrix method is developed to capture the bandgap behavior. Comprehensive analytical and experimental investigations are performed to show the benefits of introducing a certain degree of length variation in the piezoelectric transducers.

This work is organized as follows. The electromechanical equations governing the graded metamaterial system and the theoretical bandgap bounds are derived in Section 2. To directly show the superior bandgap behavior, a graded supercell structure is developed in Section 2, and the band structure is validated by the finite element model in Section 3. The effect of the spatial variation level of the piezoelectric transducers' size is then investigated in Section 3. Section 4 presents an experimental study considering different types of excitation sources to confirm the benefits of the graded design in terms of attenuation band widening as compared to the traditional piezoelectric metamaterial. Concluding remarks of this work are summarized in Section 5.

2. Theoretical Foundation

2.1 System Overview

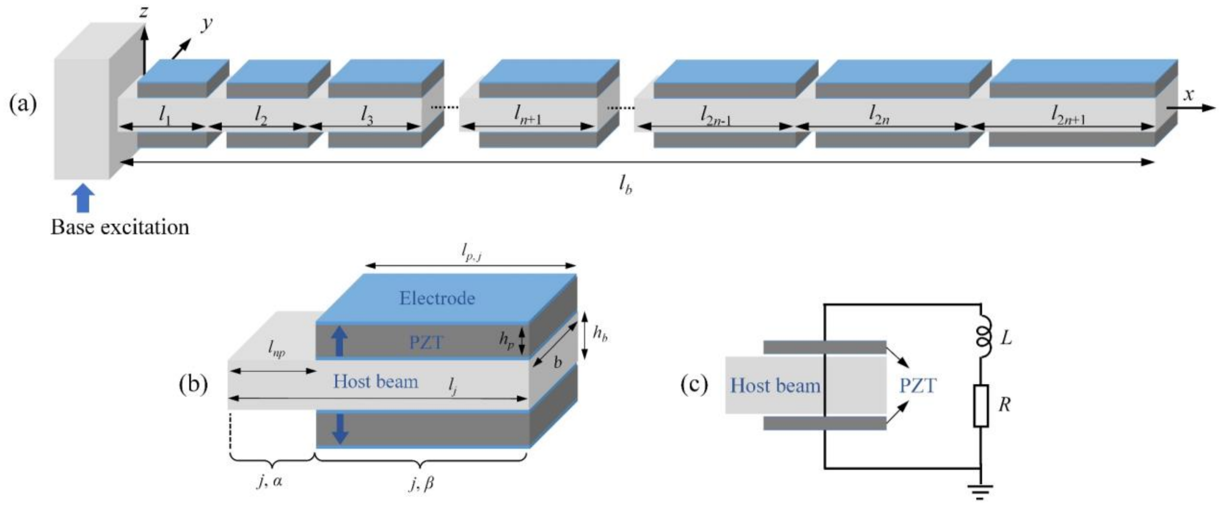

Figure 1. Design of the graded piezo-meta-beam: (a) Finitely long metamaterial beam bonded with piezoelectric transducers of grading lengths; (b) Illustration of a unit cell; (c) Shunt circuit connected to a unit cell.

Figure 1(a) shows the schematic of the graded piezoelectric metamaterial beam (for short, graded piezo-meta-beam) bonded with $2n+1$ pairs of piezoelectric transducers made of lead zirconate titanate (PZT) with different lengths in a grading pattern. The left end of the beam is clamped and subject to base excitation. The poling directions of a pair of piezoelectric transducers and the connection of their electrodes to the external shunt circuit are shown in **Figure 1(b)** and **(c)**. In this work, a resistor–inductor (R-L) circuit is considered. The beam with a total length l_b is divided into $2n+1$ segments (unit cells) of lengths l_j, $j = 1, 2, \ldots, 2n+1$ in the x-direction with one piezoelectric transducer bonded on each beam segment. The geometrical and material properties of the jth unit cell are shown in the enlarged view (**Figure 1(b)**). The portions without and with the coverage of PZT transducer in the j^{th} beam segment are marked as (j, α) and (j, β), with the lengths l_{np} and $l_{p,j}$, respectively, where $l_j = l_{p,j} + l_{np}$. Note that l_{np} is constant in each beam segment, while $l_{p,j}$ varies along the x-direction. The strict periodicity of the metamaterial, which is generally regarded as the condition for bandgap formation, is broken by the grading PZT patches with a constant spatial variation between the neighboring beam segments defined as:

$$\delta = \frac{l_j - l_{n+1}}{\left(j - (n+1)\right)} \tag{1}$$

where $l_{n+1} = l_b/(2n+1)$ is the length of the beam segment in the middle. The geometric and material properties for the graded piezo-meta-beam are listed in **Table 1**. Note that the length of each PZT patch depends on how many segments the beam is divided into and the length of the fixed length l_{np}, which will be given later.

Table 1. Geometric and material properties of piezoelectric metamaterial beam

Host beam		**PZT patch**	
Material	Aluminum	Material	PZT-5H
Thickness h_b	1 mm	Thickness h_p	1 mm
Width b	30 mm	Width b	30 mm
Length l_b	405 mm	Length $l_{p,j}$	Varying
Density ρ_b	2700 kg/m^3	Density ρ_p	7500 kg/m^3
Young's modulus E_b	69 GPa	Young's modulus in short-circuit condition E_p^{sc}	60.6 GPa
		Piezoelectric coefficient e_{31}	-16.61 C/m^2
		Permittivity ε_{33}^S	2.5554e-08 F/m

By adopting the slender beam assumption, the shear deformation and the rotatory inertia of the cross-section are neglected. Based on the Euler-Bernoulli beam theory, the governing equation of the transverse motion $w(x, t)$ of the beam is obtained:

$$\frac{\partial^2}{\partial x^2}\left[D(x)\frac{\partial^2 w(x,t)}{\partial x^2}\right] + m(x)\frac{\partial^2 w(x,t)}{\partial t^2} = 0 \tag{2}$$

where $D(x)$ and $m(x)$, respectively, denote the bending stiffness and the mass per unit area of the beam. Assuming that the PZT patches are perfectly bonded to the host beam, the bending stiffness of the *j*th beam segment can be calculated as

$$D_j(x) = \begin{cases} D_{j,\alpha} = E_b \dfrac{bh_b^{\ 3}}{12}, \ 0 \le x < l_{np} \\ D_{j,\beta} = E_b \dfrac{bh_b^{\ 3}}{12} + \dfrac{E_{p,j}(\omega) b\left[\left(h_b + 2h_p\right)^3 - h_b^{\ 3}\right]}{12}, \ l_{np} \le x < l_j \end{cases} \tag{3}$$

where E_b and $E_{p,j}$ are, respectively, the Young's modulus of the host beam and the effective Young's modulus of the *j*th PZT transducer with shunt circuit. $E_{p,j}$ can be further expressed as [42]

$$E_{p,j}(\omega) = E_p^{oc}\left(1 - \frac{k_{31}^2}{1 + i\omega C_{p,j} Z(\omega)}\right) \tag{4}$$

where $E_p^{oc} = E_p^{sc} / \left(1 - k_{31}^2\right)$ stands for the Young's modulus of the PZT patch under the open-circuit condition, and E_p^{sc} is the value under the short-circuit condition. k_{31} is the electromechanical coupling coefficient. $C_{p,j} = \varepsilon_{33}^S b \dfrac{l_{p,j}}{2h_p}$ is the internal capacitance of the PZT patch at the constant strain. It is a function of the PZT patch length $l_{p,j}$. $Z(\omega) = i\omega L + R$ is the electrical impedance of the *R*-*L* circuit. Similar to the bending stiffness, the effective mass per unit length of the beam also varies, depending on whether there is a PZT coverage or not.

$$m(x) = \begin{cases} m_\alpha = \rho_b b h_b, \ 0 \le x < l_{np} \\ m_\beta = \rho_b b h_b + 2\rho_p b h_p, \ l_{np} \le x < l_j \end{cases} \tag{5}$$

where ρ_b and ρ_p are the masses per unit length of the host beam and the PZT patch, respectively.

2.2 Attenuation Zone Estimation

The bandgap range of a uniform piezo-meta-beam is determined first to provide guidelines for estimating the attenuation zone of the graded piezo-meta-beam. It is known that bandgap behavior of piezoelectric metamaterials is affected by their bending stiffness properties [43]. From the formulation of the potential energy stored in the segments with and without PZT coverage [44], one can extract the effective bending stiffness of the *j*th unit cell:

$$D_{eff,j} = \frac{D_{j,\alpha} D_{j,\beta}}{\left(1-\chi_j\right) D_{j,\beta} + \chi_j D_{j,\alpha}} \tag{6}$$

where $\chi_j = \dfrac{l_{p,j}}{l_j} = 1 - \dfrac{l_{np}}{\delta\left(j-(n+1)\right)+l_{n+1}}$ denotes the coverage ratio of the PZT patch on the *j*th unit cell. For the graded piezo-meta-beam, χ_j and $D_{j,\beta}$ take different values for different beam segments, leading to different D_{eff}. This implies that the intentionally introduced variation of the PZT length modifies the effective bending stiffness of the composite beam along the *x*-direction, i.e., the length direction. According to the conclusions in [21], the bandgap is generated when D_{eff} becomes negative. Letting $D_{eff,j} < 0$ and solving it, one can derive the analytical bandgap of a uniform piezo-meta-beam composed of identical beam segments with the same configuration as the *j*th beam segment of the graded piezo-meta-beam:

$$\sqrt{1-\frac{k_{31}^2}{1+\gamma}}\,\omega_{LC,j} < \omega < \sqrt{1-\frac{k_{31}^2}{1+\gamma/\left(1-\chi_j\right)}}\,\omega_{LC,j} \tag{7}$$

where $\gamma = D_{j,\alpha} \big/ D_p^{sc}$ and $D_p^{sc} = E_p^{sc} b\left[\left(h_b+2h_p\right)^3 - h_b^3\right]\big/12$ is the bending stiffness of the piezoelectric transducer under the short-circuit condition (i.e., R = 0). $\omega_{LC,j} = 1\big/\sqrt{LC_{p,j}}$ is the resonance frequency of the *L*-*C* circuit formed by the internal capacitor of the PZT patch and the shunted inductor. Based on Eq. (7), **Figure 2** shows the variation of the normalized bandgap region with different piezoelectric coverage ratios χ. The other parameters of the system are listed in **Table 1**. It can be seen that the upper bound of the bandgap decreases rapidly with the decrease of the coverage ratio χ, while the lower bound remains constant.

Additionally, it is also noticed that when $\chi \to 1$, the upper bound of the bandgap approaches the resonant frequency $\omega_{LC,j}$ of the shunted PZT (i.e., $\omega/\omega_{LC,j} = 1$), which can also be mathematically proved by taking the limit of the upper bound in Eq. (7):

$$\lim_{\chi_j \to 1} \left(\sqrt{1 - \frac{k_{31}^2}{1+\gamma/\left(1-\chi_j\right)}} \omega_{LC,j} \right) = \omega_{LC,j} \tag{8}$$

In this way, Eq. (7) is reduced to the bandgap expression derived in [45] for the sandwich-type metamaterial with fully covered piezoelectric layers.

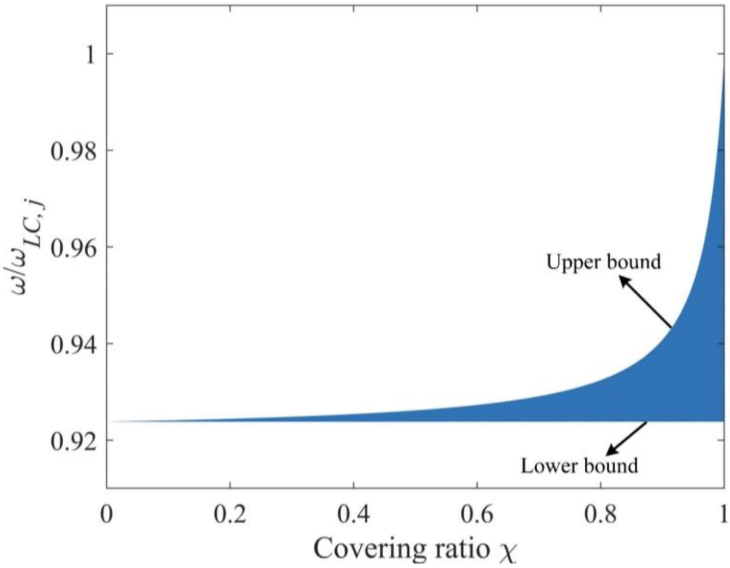

Figure 2. Variation of the normalized bandgap bounds with the change of the piezoelectric coverage ratio χ .

For the “graded” design, the grading manner is achieved by defining a constant spatial variation δ, which makes the effective bending stiffness of the beam segment vary progressively. Therefore, it can be speculated that the bending stiffnesses of the unit cells spatially distributed along the beam will become negative in different frequency ranges, resulting in an array of discrete attenuation zones. To facilitate the analysis, we rewrite $C_{p,j}$ in terms of the capacitance of the PZT in the middle, i.e., $C_{p,n+1}$:

$$C_{p,j} = \left[\left(\delta\left(j-n-1\right)\right)/l_{p,n+1} + 1\right] C_{p,n+1} \tag{9}$$

Combining with Eq. (9), $\omega_{LC,j}$ can be re-expressed in terms of $\omega_{LC,n+1}$

$$\omega_{LC,j} = \frac{1}{\sqrt{\left(\delta\left(j-n-1\right)\right)/l_{p,n+1}+1}}\omega_{LC,n+1} \tag{10}$$

From Eq. (10), it can be found that when $\delta > 0$, namely, the PZT length gradually increases along the x-direction, the resonant frequency array $\omega_{LC,j}, j=1,2,\ldots,2n+1$ is arranged in descending order (i.e., $\omega_{LC,1} > \omega_{LC,2} > \ldots > \omega_{LC,n+1} > \ldots > \omega_{LC,2n+1}$). Consequently, a series of attenuation regions related to these resonance frequencies will be produced in descending order in the frequency spectrum. When $\delta < 0$, namely, the PZT length shrinks along the x-direction, the above trend is opposite. In these two cases, $\omega_{LC,n+1}$ is always at the center of the resonant frequency array. By combining with Eq. (7), the overall attenuation zone of the graded piezo-meta-beam can be predicted by Eq. (11) and will be verified later in Section 3.1. Due to the geometric symmetry, the estimated attenuation zone boundary related to $\delta < 0$ is numerically equal to that of $\delta > 0$.

$$\sqrt{1-\frac{k_{31}^2}{1+\gamma}}\frac{1}{\sqrt{1+\frac{n\delta}{l_{p,n+1}}}}\omega_{LC,n+1} < \omega < \sqrt{1-\frac{k_{31}^2}{1+\gamma/\left(1-\chi_1\right)}}\frac{1}{\sqrt{1-\frac{n\delta}{l_{p,n+1}}}}\omega_{LC,n+1} \text{ for } \delta > 0 \tag{11}$$

2.3 Analytical Solution

To quantify the effect of the grading PZT patches on the wave propagation in the metamaterial beam, the transfer matrix method is employed to calculate the dynamic response and dispersion relation of the graded piezo-meta-beam. By assuming the steady-state response as $w(x, t) = W(x)e^{i\omega t}$, the general solution to Eq. (2) in the jth beam segment can be written in the form of

$$W_{j,\lambda}\left(x\right) = \mathbf{H}_{j,\lambda}\mathbf{\Psi}_{j,\lambda} \text{ for } \lambda = \alpha,\beta \tag{12}$$

where $\mathbf{H}_{j,\lambda}=\left[\cos\left(k_{j,\lambda}x\right),\sin\left(k_{j,\lambda}x\right),\cosh\left(k_{j,\lambda}x\right),\sinh\left(k_{j,\lambda}x\right)\right]$, with

$$k_{j,\lambda}=\sqrt[4]{\omega^2\frac{m_\lambda}{D_{j,\lambda}}} \tag{13}$$

and $\boldsymbol{\Psi}_{j,\lambda}=\left[\bar{A}_{j,\lambda},\bar{B}_{j,\lambda},\bar{C}_{j,\lambda},\bar{D}_{j,\lambda}\right]^{\mathrm{T}}$ is the coefficient vector to be determined. Considering the continuity boundary conditions of the displacement, rotation angle, bending moment, and shear force at the interface between beam segments (*j*, *α*) and (*j*, *β*), one can obtain

$$\begin{aligned} &W_{j,\alpha}\left(l_{np}\right)=W_{j,\beta}\left(0\right) && W'_{j,\alpha}\left(l_{np}\right)=W'_{j,\beta}\left(0\right)\\ &D_{j,\alpha}W''_{j,\alpha}\left(l_{np}\right)=D_{j,\beta}IW''_{j,\beta}\left(0\right) && D_{j,\alpha}W'''_{j,\alpha}\left(l_{np}\right)=D_{j,\beta}W'''_{j,\beta}\left(0\right)\end{aligned} \tag{14}$$

Similarly, at the interface between segments (*j*, *β*) and (*j*+1, *α*), the continuity conditions are

$$\begin{aligned} &W_{j,\beta}\left(l_{p,j}\right)=W_{j+1,\alpha}\left(0\right) && W'_{j,\beta}\left(l_{p,j}\right)=W'_{j+1,\alpha}\left(0\right)\\ &D_{j,\beta}W''_{j,\beta}\left(l_{p,j}\right)=D_{j+1,\alpha}W''_{j+1,\alpha}\left(0\right) && D_{j,\beta}W'''_{j,\beta}\left(l_{p,j}\right)=D_{j+1,\alpha}W'''_{j+1,\alpha}\left(0\right)\end{aligned} \tag{15}$$

where $l_{p,j}=\delta\left(j-\left(n+1\right)\right)+l_b/\left(2n+1\right)-l_{np}$. Substituting Eq. (12) into Eqs. (14) and (15), respectively, then rewriting them into matrix form, one can obtain the transfer relationship between the *j*th and (*j*+1)th unit cells as

$$\boldsymbol{\Psi}_{j+1,\alpha}=\mathbf{T}_j\boldsymbol{\Psi}_{j,\alpha} \tag{16}$$

with the transfer matrix being:

$$\mathbf{T}_j=\mathbf{H}_{j+1,\alpha}(0)^{-1}\mathbf{H}_{j,\beta}\left(l_{p,j}\right)\mathbf{H}_{j,\beta}\left(0\right)^{-1}\mathbf{H}_{j,\alpha}\left(l_{np}\right) \tag{17}$$

in which

$$\mathbf{H}_{j,\lambda}\left(x\right)=\begin{bmatrix}\cos\left(k_{j,\lambda}x\right) & \sin\left(k_{j,\lambda}x\right) & \cosh\left(k_{j,\lambda}x\right) & \sinh\left(k_{j,\lambda}x\right)\\ -k_{j,\lambda}\sin\left(k_{j,\lambda}x\right) & k_{j,\lambda}\cos\left(k_{j,\lambda}x\right) & k_{j,\lambda}\sinh\left(k_{j,\lambda}x\right) & k_{j,\lambda}\cosh\left(k_{j,\lambda}x\right)\\ -D_{j,\lambda}k_{j,\lambda}^{2}\cos\left(k_{j,\lambda}x\right) & -D_{j,\lambda}k_{j,\lambda}^{2}\sin\left(k_{j,\lambda}x\right) & D_{j,\lambda}k_{j,\lambda}^{2}\cosh\left(k_{j,\lambda}x\right) & D_{j,\lambda}k_{j,\lambda}^{2}\sinh\left(k_{j,\lambda}x\right)\\ D_{j,\lambda}k_{j,\lambda}^{3}\sin\left(k_{j,\lambda}x\right) & -D_{j,\lambda}k_{j,\lambda}^{3}\cos\left(k_{j,\lambda}x\right) & D_{j,\lambda}k_{j,\lambda}^{3}\sinh\left(k_{j,\lambda}x\right) & D_{j,\lambda}k_{j,\lambda}^{3}\cosh\left(k_{j,\lambda}x\right)\end{bmatrix} \tag{18}$$

For the graded piezo-meta-beam with $2n+1$ unit cells, the transfer relationship between the left end of the 1st segment and the right end of the $(2n+1)$th segment can be obtained by repeating the above procedure:

$$\mathbf{\Psi}_{2n+1,\beta}=\mathbf{H}_{2n+1,\beta}(0)^{-1}\mathbf{H}_{2n+1,\alpha}\left(l_{np}\right)\left(\prod_{j=1}^{2n}\mathbf{T}_{j}\right)\mathbf{\Psi}_{1,\alpha} \tag{19}$$

To calculate the vibration transmissivity from the left end of the graded piezo-meta-beam to the right end, a unit harmonic displacement $u_0(t)=e^{i\omega t}$ is applied at the left end as the excitation. The clamped-free boundary condition of the beam yields

$$\begin{aligned} &W_{1,\alpha}\left(0\right)=1 && W_{1,\alpha}'\left(0\right)=0\\ &D_{2n+1,\beta}W_{2n+1,\beta}''\left(l_{p,2n+1}\right)=0 && D_{2n+1,\beta}W_{2n+1,\beta}'''\left(l_{p,2n+1}\right)=0 \end{aligned} \tag{20}$$

Combining Eqs. (12), (19) and (20) yields

$$\begin{bmatrix}\mathbf{H}_{1,\alpha}(0)_{1,:} & \mathbf{0}\\ \mathbf{H}_{1,\alpha}(0)_{2,:} & \mathbf{0}\\ \mathbf{0} & \mathbf{H}_{2n+1,\beta}\left(l_{p,2n+1}\right)_{3,:}\\ \mathbf{0} & \mathbf{H}_{2n+1,\beta}\left(l_{p,2n+1}\right)_{4,:}\\ \mathbf{H}_{2n+1,\beta}(0)^{-1}\mathbf{H}_{2n+1,\alpha}\left(l_{np}\right)\left(\prod_{j=1}^{2n}\mathbf{T}_{j}\right) & -\mathbf{I}\end{bmatrix}\begin{bmatrix}\mathbf{\Psi}_{1,\alpha}\\ \mathbf{\Psi}_{2n+1,\beta}\end{bmatrix}=\begin{bmatrix}1\\0\\0\\0\\ \mathbf{0}\end{bmatrix} \tag{21}$$

where $\mathbf{H}_{j,\lambda}(x)_{1,:}$ denotes the 1st row of $\mathbf{H}_{j,\lambda}(x)$ and **I** is the 4×4 identity matrix. By solving Eq. (21), i.e., an 8×8 matrix, one can obtain the coefficient matrix $\mathbf{\Psi}_{2n+1,\beta}$. The transmittance of the piezo-meta-beam can be calculated as

$$\tau(\omega) = 20\log_{10}\left|\hat{W}_{2n+1,\beta}\left(l_{p,2n+1}\right)\right| \qquad \text{(dB)} \tag{22}$$

where $\hat{W}_{2n+1,\beta}(l_{p,2n+1}) = \mathbf{H}_{2n+1,\beta}\left(l_{p,2n+1}\right)_{1,:}\boldsymbol{\Psi}_{2n+1,\beta}$ denotes the normalized displacement at the right end of the beam.

To capture the bandgap behavior, dispersion relation analysis of an infinite period structure is usually a powerful method. However, the PZT patch length variation breaks the periodicity, resulting in the dispersion relation described by the Floquet-Bloch theorem no longer existing. Therefore, a supercell graded metamaterial structure is proposed by taking the (2*n*+1) cells as a superlattice cell. The Bloch boundary condition can then be applied to the supercell:

$$\boldsymbol{\Psi}_{2n+2,\alpha} = e^{iqd}\boldsymbol{\Psi}_{1,\alpha} \tag{23}$$

where $q^* = qd/\pi$ is the wave propagation constant (dimensionless). Note that q^* is normally a complex value. The real part of q^*, i.e., RE(q^*), is the wavenumber, and the imaginary part of q^*, i.e., IM(q^*), represents the attenuation factor, which indicates the attenuation strength. $d = l_b$ is the lattice constant of the superlattice cell. To satisfy Eqs. (16) and (23) simultaneously, an eigenvalue problem is raised:

$$\left[\left(\prod_{j=1}^{2n}\mathbf{T}_j\right) - e^{iqd}\mathbf{I}\right]\boldsymbol{\Psi}_{1,\alpha} = 0 \tag{24}$$

3. Band Structure and Transmittance Analysis

3.1 Band Structure Behavior

In this section, we comprehensively investigate the bandgap behavior of the piezo-meta-beam with grading piezoelectric transducers. First, the supercell band structure analysis is conducted. An undamped supercell consisting of 9 (i.e., $n = 4$) segments with spatially varying bimorph PZT patches (hereinafter referred to as the graded supercell for short) is considered. The length of the beam segment in the middle is set to be $l_{n+1} = 45$ mm, and the lattice constant of the supercell is $d = (2n+1)\times l_{n+1} = 405$ mm. A small gap ($l_{np} = 5$ mm) between the neighboring PZT patches is set to ensure a large piezoelectric coverage ratio. It implies that the length of the PZT in the middle is $l_{p,n+1} = l_{n+1} - l_{np} = 40$ mm. The spatial variation is set to be $\delta = 2$ mm. The inductor has a value of $L = 6.6$ H. Thus, the LC circuit resonance frequency of the middle piezoelectric element is $f_{LC,\,n+1} = 500$ Hz. The other material and geometrical parameters are listed in **Table 1**. For the same given parameters, a finite element model is also established using COMSOL Multiphysics for comparison and verification. It is worth mentioning that to match the assumption we made in developing the theoretical model, the three-dimensional material tensor of the piezoelectric material in COMSOL is modified to ensure that PZT transducers only operate in the 31-mode, as given below:

$$\mathbf{C}_{\mathbf{E}} = E_p^{sc}\mathbf{I}_{6\times 6},\quad \mathbf{e} = \begin{bmatrix} \mathbf{0} & \mathbf{0} \\ e_{31} & \mathbf{0} \end{bmatrix},\quad \boldsymbol{\varepsilon}^{\mathrm{S}} = \left[0, 0, \varepsilon_{33}^{S}\right] \tag{25}$$

where $\mathbf{C}_{\mathbf{E}}$, $\mathbf{e}$ and $\boldsymbol{\varepsilon}^{\mathrm{S}}$, are, respectively, the elastic matrix, the coupling matrix and the permittivity vector. $e_{31} = d_{31}E_p^{sc}$ is the piezoelectric coefficient in the 31-mode. **Figure 3(c)** shows the band structure of the undamped graded supercell. The band structures of the supercell containing 9 uniform segments (uniform supercell, for short) (**Figure 3(b)**) and an ordinary unit-cell (**Figure 3(a)**) are also provided for comparison. The beam segment lengths of the two uniform models are chosen to be the same as that of the middle segment of the grading design, i.e., l_{n+1}. Hence, the lattice constants of the two uniform models are d and l_{n+1}, respectively, implying that the wavenumber for the ordinary unit-cell is $q^* = ql_{n+1}/\pi$. **Figure 3** compares the results from the theoretical models and the finite element simulation. Black and red dots denote theoretical and FE results, respectively. Blue- and green-shaded areas denote LR and Bragg bandgaps, respectively. It is shown that the two results are highly consistent with each other.

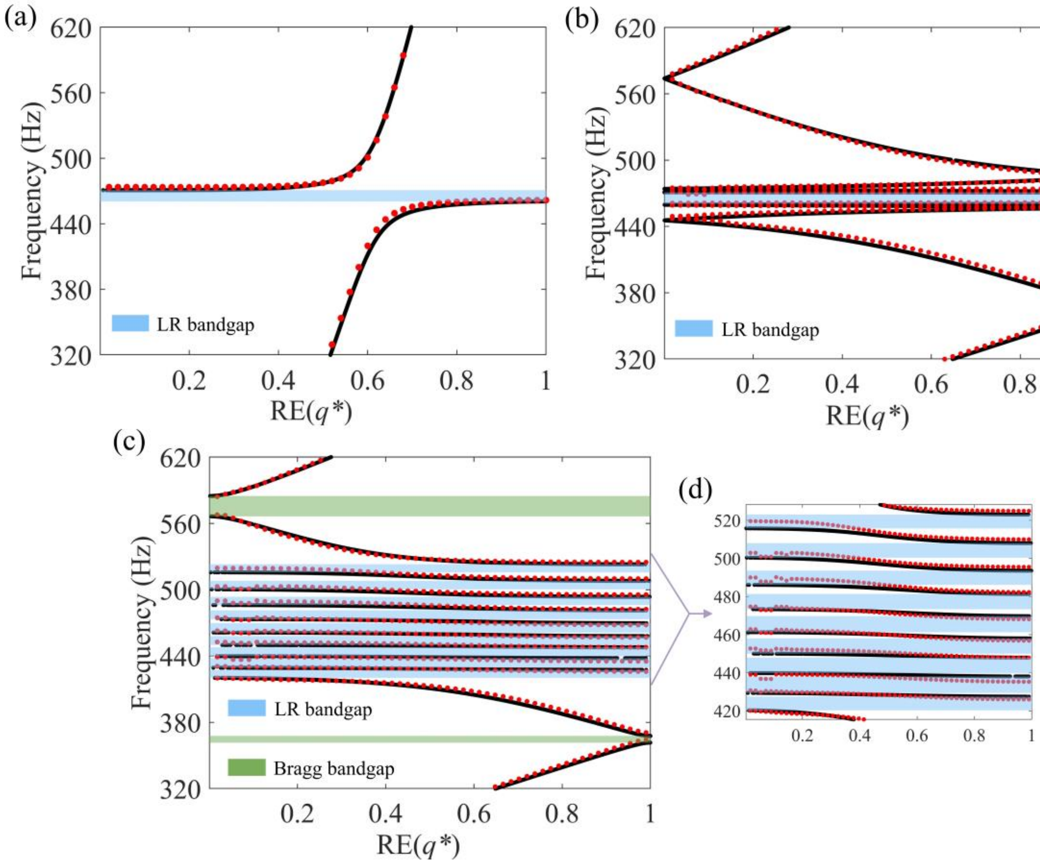

Figure 3.Band structure of the (a) unit-cell structure; (b) uniform supercell structure; (c) graded supercell structure configured with $\delta = 2$ mm. Black and red dots denote the theoretical and FE results, respectively. The blue-shaded areas denote the LR bandgaps, and the green-shaded areas are the Bragg bandgaps. To clearly show the discrete bandgaps, the LR bandgap region of (c) is further enlarged, as shown in (d).

The color shaded areas represent bandgaps, i.e., the frequency ranges where no pure real wavenumbers exist. Since the supercell contains multiple sub-cells and due to the band folding effect in the reduced supercell Brillouin zone [46], the number of the dispersion curves of the uniform supercell (**Figure 3(b))** is more than that of the unit-cell (**Figure 3(a)**), but this band folding effect does not affect the width of LR bandgap, i.e., the region induced by the circuit resonance shaded in blue. In comparison, it can be noted that multiple LR bandgaps are produced in the band structure of the graded supercell (**Figure 3(c)**), spreading over higher and lower frequency ranges. As discussed in Section 2.2, these discrete bandgaps are induced by the negative bending stiffness segments distributed along the beam in the "grading" pattern. The width of the discrete bandgaps sums up to 70.5 Hz, which is about 7 times that of the uniform counterpart, i.e., 10.2 Hz. Moreover, due to the band folding effect and the aperiodicity caused by the "graded" design, two Bragg bandgaps emerge at the folding points of the band structure. This phenomenon agrees well with the reported results of aperiodic metastructures [47]. In addition, multiple flat passbands appear between the neighboring LR bandgaps, as shown in **Figure 3(c)** and the enlarged view in **Figure 3(d)**. Waves within the passbands can propagate through the beam. Thus, the appearance of passbands is detrimental to broadband vibration attenuation.

To get more insights into the vibration attenuation capacity of the graded piezo-meta-beam, we plot the transmittance heatmap for a finitely long model of the graded piezo-meta-beam versus the excitation frequency and the beam location in **Figure 4(a)**. This finitely long model is obtained by replacing the Floquet-Bloch boundary condition applied to the two ends of the supercell with the clamped-free boundary condition. The transmittance heatmap for the uniform counterpart piezo-meta-beam is also plotted in **Figure 4(b)** for comparison.

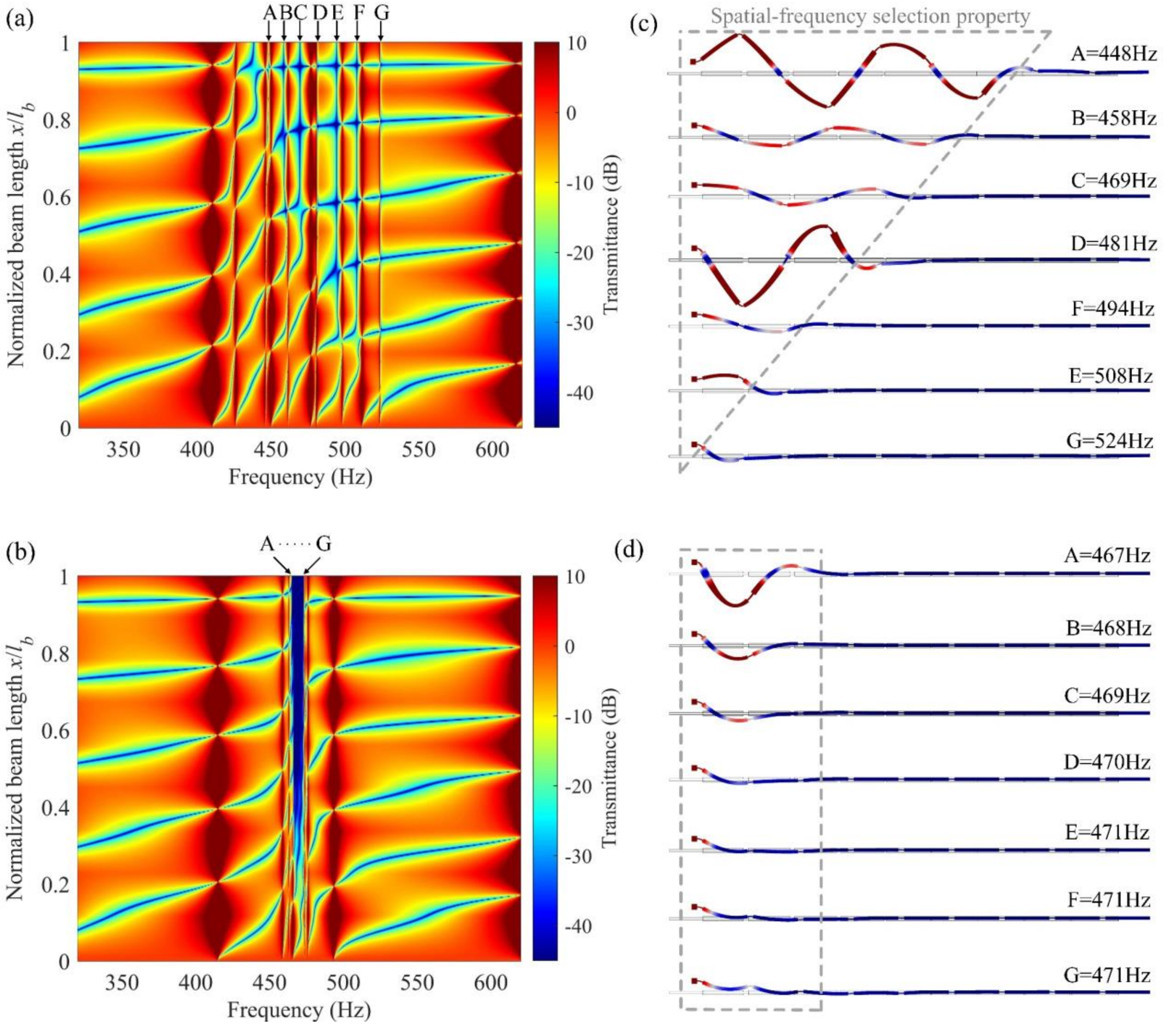

Figure 4. Transmittance heatmaps associated with the beam length and frequency of (a) finitely long graded piezo-meta-beam and (b) finitely long uniform piezo-meta-beam; Vibration modes at selected frequencies marked as A, B,…,G of (c) finitely long graded piezo-meta-beam and (d) finitely long uniform piezo-meta-beam. It is noted that the spatial-frequency selection property is observed inside the triangular dashed box in (c), while it is not obvious in the rectangular dashed box in (d).

Similar to the band structure analysis result, **Figure 4(a)** shows that the vibration attenuation region of the graded piezo-meta-beam occurs in a wider but discontinuous frequency range as compared to that of the uniform one (**Figure 4(b)**). Vibration modes of the uniform and graded piezo-meta-beams at the marked frequencies A, B,…, G within the attenuation regions are respectively plotted in **Figure 4(c)** and **(d)**. It is revealed in **Figure 4(c)** that the wave propagation in the graded piezo-meta-beam exhibits a spatial-frequency selection property. Specifically, as indicated in the triangular dashed box in **Figure 4(c)**, the vibration energy becomes more concentrated at the clamped end of the metamaterial beam as the excitation frequency increases. This phenomenon is also referred to as "rainbow trapping" [48, 49]. In contrast, the wave trapping phenomenon did not occur in the uniform piezo-meta-beam, and the vibration is evenly attenuated along the wave propagation direction. It is worth noting that the attenuation region identified in **Figure 4(a)** cannot perfectly match the discrete LR bandgaps shown in **Figure 3(c)**, since the finitely long model (the standing wave system) is actually different from the infinitely long model (traveling wave system), and we consider only a single supercell [50]. Increasing the number of supercells will make the transmittance profile better match the band structure result.

The above analysis is conducted in the absence of damping. In practice, electrical damping induced by the parasitic resistance of the shunt circuit is unavoidable, which will be demonstrated in the experiments later. We considered the existence of a resistor of $R = 200\ \Omega$ to investigate the electrical damping effect on vibration attenuation. **Figure 5(a)** presents the dimensionless wavenumber: RE(q^*). It is the same as **Figure 4(a)**, indicating that resistors do not affect the locations of bandgaps. The imaginary part of the wave propagation constant, i.e., the attenuation factor, is plotted in **Figure 5(b)**. Interestingly, one can observe that due to the resistance-induced damping, the attenuation factors are non-zero in the flat passband regions, leading to a board continuous attenuation zone. It should be noted that pure real/imaginary q^* does not exist for damped periodic structures. The calculated imaginary values are extracted from the complex wave propagation constant, representing the evanescent waves. Consequently, the vibration amplitude in this scenario is suppressed by both the energy dissipation effect and the local resonance mechanism.

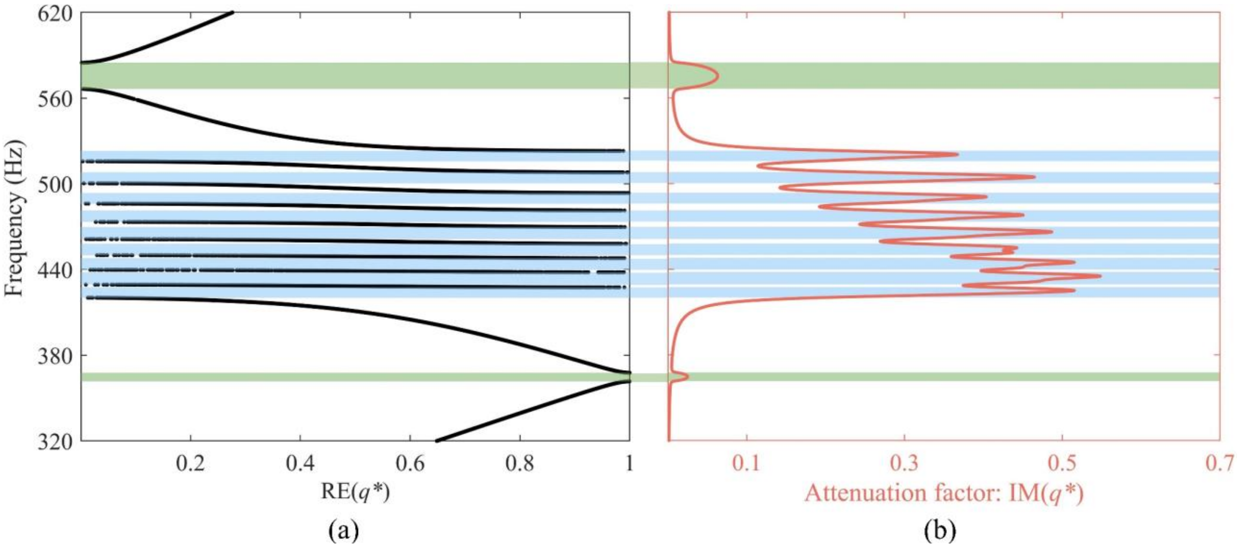

Figure 5. Complex band structure of the graded supercell structure in the case of $R = 200\ \Omega$: (a) the dimensionless wavenumber; (b) the imaginary part of dimensionless wave propagation constant, i.e., the attenuation factor. A continuous attenuation factor appears due to the electrical damping.

Figure 6(a) depicts the evolution of the attenuation factor of the graded piezo-meta-beam in the heatmap when R varies from 1 Ω to 500 Ω. When R is minor, multiple dark blue areas alternate with dark red areas, indicating that the attenuation region is discontinuous. As R increases, the dark blue areas vanish, and a continuous attenuation region forms. For example, the smallest attenuation factor in the green highlighted area is more than 0.1 when $R > 174.5\ \Omega$. The bandgap bounds of the graded piezo-meta-beam estimated by Eq. (11) are also marked in **Figure 6(a)**, showing a good agreement with the attenuation factor heatmap result at a large R. In addition, the attenuation factors in the original bandgap regions decrease when R increases because the electrical damping weakens the local resonance effect.

Based on the band structure analyses, we have demonstrated the possibility of realizing broadband vibration attenuation with the proposed graded piezo-meta-beam. For a finitely long metamaterial beam, **Figure 6(b)** shows the transmittances of the graded piezo-meta-beam when $R = 10\ \Omega$ and $R = 200\ \Omega$. As the resistance increases, the resonant peaks in the flat passbands (marked by circles) are significantly suppressed. At the same time, a larger resistance also weakens the attenuation ability in the bandgaps, i.e., the attenuation valleys become shallower. This is in good agreement with the discussion on the complex band structure. Although the electrical damping effect has suppressed the resonant peaks, the attenuation regions in the form of valleys remain discontinuous. This may attribute to the mistuned spatial variation ($\delta = 2$ mm). As discussed before, the electrical parameters of the shunted piezoelectric transducers with varying lengths are different, which results in an array of discrete attenuation zones. If the spatial variation δ is over-tuned, the discrete bandgaps generated by those unit cells cannot overlap, and the vibration attenuation zones will be too dispersed in the frequency spectrum. Hence, it is necessary to investigate the tuning characteristics of the vibration attenuation region with the change of δ. Hereafter, we fix the resistance $R = 200\ \Omega$ and will discuss the effect of δ on the vibration attenuation region in the following section.

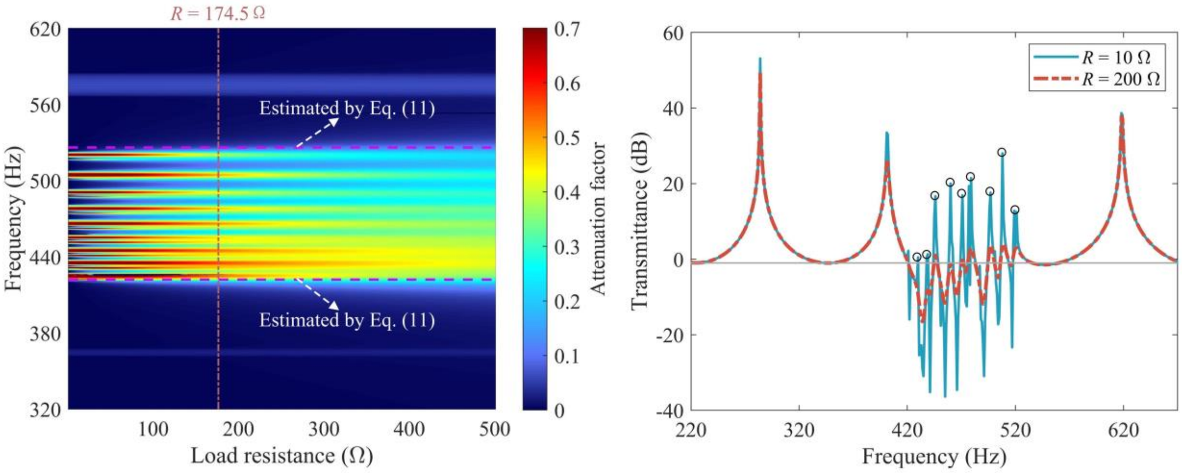

(a) (b)

Figure 6. (a) Evolution of the attenuation factor heatmap of the graded supercell structure with varying load resistance (1Ω - 500Ω); (b) Comparison of tip transmittances of the finitely long graded piezo-meta-beam in the cases of $R = 10\ \Omega$ and $R = 200\ \Omega$.

3.2 Transmittance Evolution

With the same parameters, **Figure 7(a)** shows the transmittance heatmap of the graded piezo-meta-beam as the function of the spatial variation δ. Note that $\delta = 0$ indicates the conventional uniform piezo-meta-beam. The areas where the transmittance is less than 0 dB refer to the attenuation zones. As shown in **Figure 7(a)**, the transmittance heatmap is nearly symmetrical with respect to $\delta = 0$. It can also be observed that the attenuation capability is sensitive to δ. Even a small variation ($\delta = 0.2$ mm, for example) may significantly decrease the attenuation capability. By increasing $|\delta|$, the attenuation zone becomes wider, extending to the higher and lower frequency ranges. Notably, when $\delta > 1.04$ mm and $\delta < -0.86$, multiple fractured attenuation regions appear. As mentioned in the previous subsection, these fractured attenuation regions attribute to the overdispersion of the attenuation regions generated by the piezoelectric elements in the frequency spectrum. To show more details, **Figure 7(b)** displays the transmittance profiles of the graded piezo-meta-beam at several values of δ. In other words, the curves in **Figure 7(b)** are the slice views of **Figure 7(a)**. The color-filled region refers to the dominant attenuation zone, i.e., the widest continuous valley. It is further confirmed that increasing $|\delta|$ leads to extending the attenuation zone, while excessively increasing δ will split the attenuation zone into pieces.

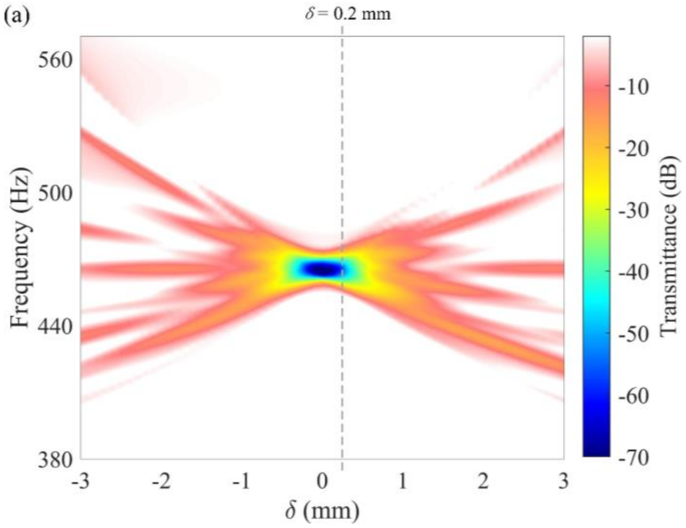

(b)

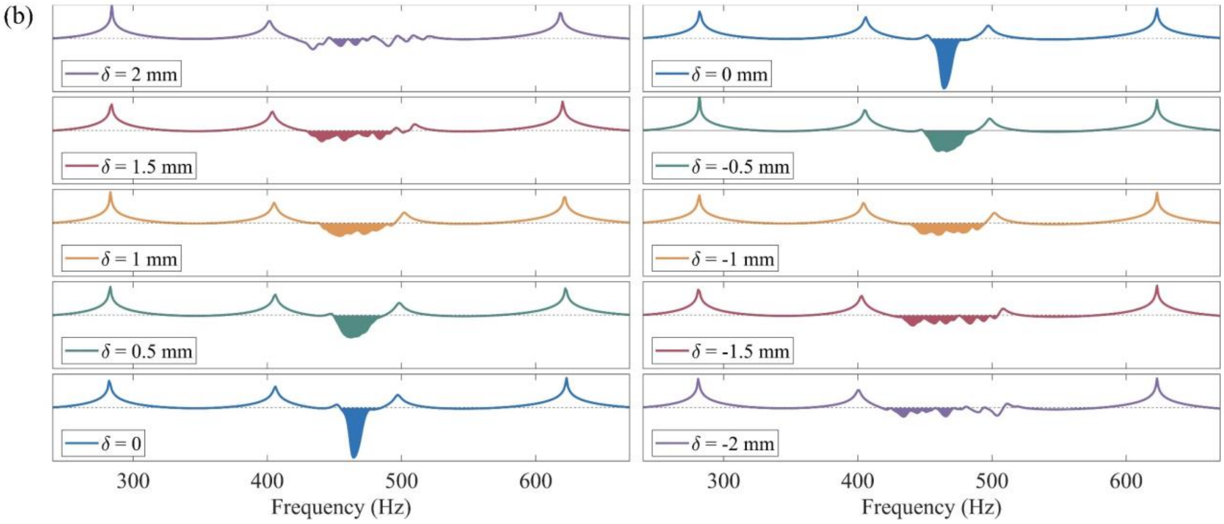

Figure 7. (a) Heatmap of the evolution of the transmittance of the graded piezo-meta-beam with varying spatial variation δ; (b) Transmittances of the graded piezo-meta-beam with a few specific δ, where the color-filled regions are the dominant attenuation zones.

4. Experimental Study

4.1 Experimental Setup

The left-hand side in **Figure 8(a)** shows the fabricated graded piezo-meta-beam. A uniform piezo-meta-beam, as shown on the right-hand side of **Figure 8(a)**, is also fabricated for comparison. These piezo-meta-beams are made of aluminum alloy and contain 9 bimorph PZT-5H pairs. One end of the beam is clamped on a 3D-printed fixture. **Figure 9** shows the experimental setup for conducting the vibration test. The entire vibration test system consists of two permanent magnet shakers (Labworks, model: ET-132-203), a shaker amplifier (SignalForce, model: PA30E), several accelerometers (PCB piezotronics, model: 352C22), a vibration controller (VibrationResearch, model: VR9500), and a DC power supply (ESCORT, model: EPS-3060TD). The excitation is applied at the clamped end of the piezo-meta-beams. One accelerometer is attached to each end of the piezo-meta-beam to measure the frequency response. The input signal is controlled by VibrationVIEW 2021 (the vibration controller software), and the vibration data are recorded by the vibration controller. Two types of vibration tests, i.e., harmonic and random excitation tests, are performed to evaluate the vibration attenuation performance of the developed graded piezo-meta-beam in comparison with its uniform counterpart.

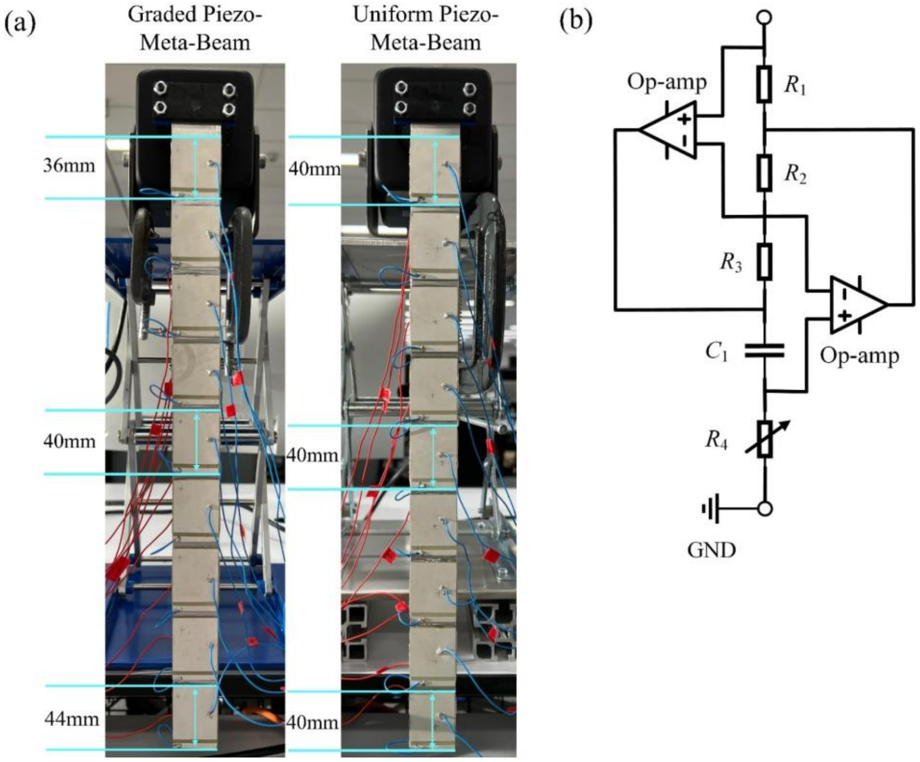

Figure 8. (a) Prototyped piezo-meta-beams; (b) Diagram of the synthetic inductor circuit.

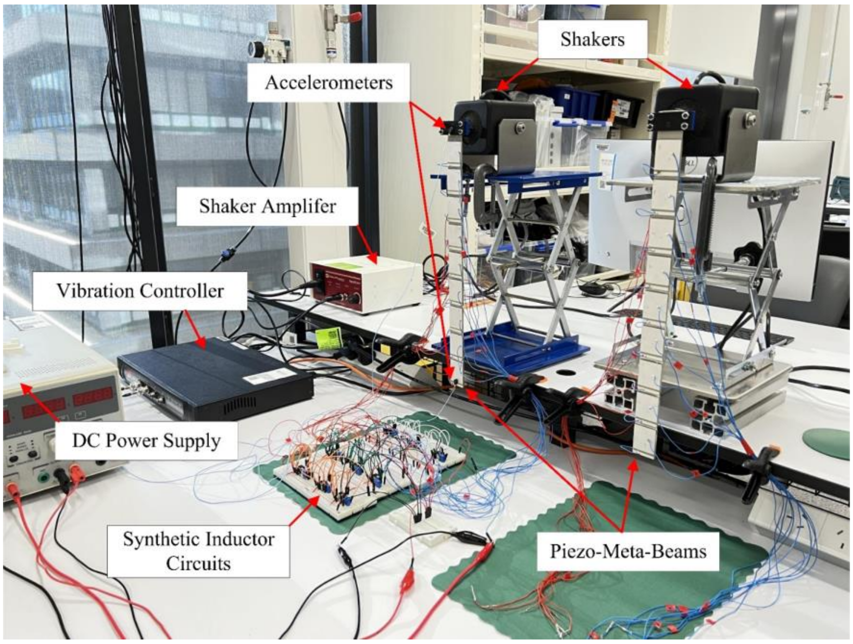

Figure 9. Experimental setup of vibration tests.

4.2 Result Discussion

For the graded piezo-meta-beam, a spatial variation $\delta = 1$ mm is chosen, which means the PZT patches are of different lengths 36mm, 37 mm,…, 43 mm, and 44 mm. For the uniform piezo-meta-beam, PZT patches of the same length 40 mm (i.e., $\delta = 0$ mm) are used. The first beam segment without PZT coverage near the clamped end is slightly longer than the segments elsewhere to ensure that the fixture will not damage the nearest PZT patch. The internal capacitances of the above two groups of bimorph PZT pairs adhered to the graded and uniform piezo-meta-beams are measured by a multimeter, and their values are listed in **Table 2**. It is worth noting that the capacitances of the PZT pairs in the uniform piezo-meta-beam are not perfectly identical due to the machining error. The subscript $j = 1, 2, \ldots, 9$ denotes the index of the PZT pair from the clamped end to the free end. It can be seen that the capacitance varies with the change of the PZT patch length. All the PZT patches are adhered to the host beam using electrically insulative epoxy. The other geometric and material parameters of the physical prototype tested in the experiment are the same as those listed in **Table 1**.

Table 2. Capacitances of PZT pairs in the experiment (the unit is nF).

	$C_{p,1}$	$C_{p,2}$	$C_{p,3}$	$C_{p,4}$	$C_{p,5}$	$C_{p,6}$	$C_{p,7}$	$C_{p,8}$	$C_{p,9}$
Graded piezo-meta-beam	13.06	13.35	13.78	14.36	15.27	15.86	16.43	16.89	17.73
Uniform piezo-meta-beam	15.55	15.49	15.42	15.56	15.47	15.56	15.70	15.38	15.49

Since the inherent capacitance of the PZT patch is small, a large inductor with a relatively small parasitic resistance is desired to generate the resonance around the expected frequency while avoiding excessive resistance to weaken the resonance effect. In this experiment, the inductors are realized using Antoniou's synthetic inductor circuits [51], as depicted in **Figure 8(b)**. Based on the characteristics of the op-amp, the equivalent inductance can be calculated as

$$L = \frac{R_1 R_3 R_4}{R_2} C_1 \tag{26}$$

LM358 op-amps with an operating range up to ± 32 V are used as amplifiers. R_4 is a variable resistor ranging from 0 to 50 kΩ. The other electrical parameters used in the synthetic circuit are listed in **Table 3**.

Table 3. Circuital parameter of the synthetic inductor.

	Symbol	Value/Model
Capacitor	C_1	100 nF
Resistor	R_1	10 kΩ
Resistor	R_2	2.2 kΩ
Resistor	R_3	10 kΩ
Resistor	R_4	50 kΩ (variable)
Op-amp		LM358

Note that there is no need to add any auxiliary resistor to flatten the undesired resonance peaks since a parasitic resistance unavoidably exists in the synthetic circuit due to the non-idealities of the practical op-amps [52]. The synthetic inductor circuit can be regarded as an in-series connected R-L circuit. However, the parasitic resistance cannot be measured directly because the synthetic inductor circuit is an active circuit. Alternatively, a fully charged capacitor C_f = 16 nF with an initial voltage of U_c = 11V is connected to the synthetic inductor circuit. According to the R-L-C oscillation, the voltage V_c across the capacitor will decay exponentially with respect to time t, which can be calculated as

$$V_c = \pm \left| \frac{1}{2} U_c e^{-t/\tau} \right| \tag{27}$$

where $\tau = 2L/R_p$ is the time constant, and R_p is the series resistance. **Figure 10(a)** shows the measured voltage V_c across the capacitor versus time. The equivalent impedance L is set to 39.58 H, corresponding to the LC resonant frequency of f_{LC} = 200 Hz. The theoretical V_c based on Eq. (27) when $R_p = 320\ \Omega$ is also plotted in **Figure 10(a)**. The result matches the measured one well, implying that the parasitic resistance is around 320 Ω. Then, multiple inductances L, corresponding to $f_{LC} = 300, 400, \ldots, 700$ Hz, are considered. By repeating the above procedure, one can estimate their corresponding parasitic resistances. The relationship between the parasitic resistance and the equivalent inductance is shown in **Figure 10(b).** It can be found that the parasitic resistance increases with the increase of the equivalent inductance.

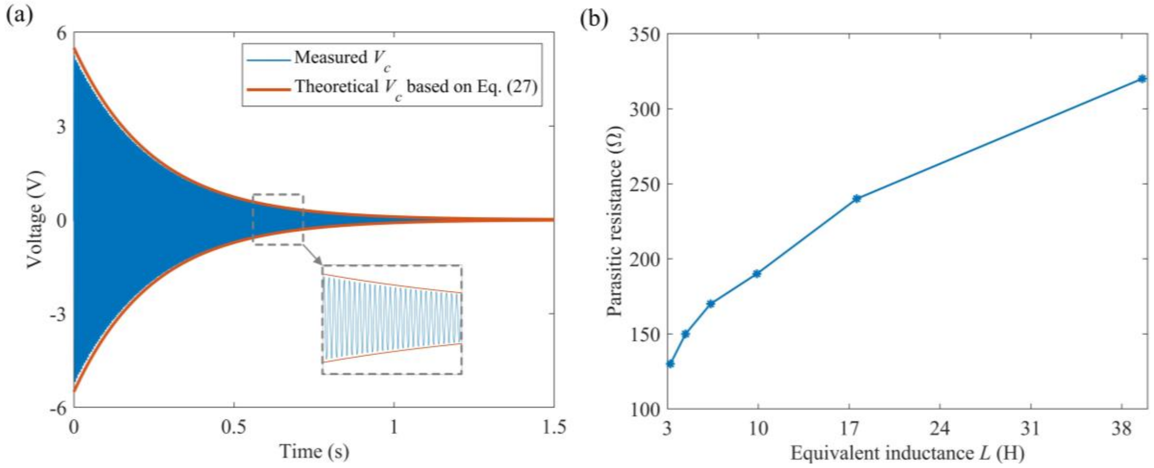

Figure 10. (a) Comparison of the measured and theoretical voltage V_c of the *R-L-C* circuit with $L = 39.58$ H, $C_f = 16$ nF, and $R_p = 320\ \Omega$. The theoretical result matches the measured one well when $R_p = 320\ \Omega$, implying that the parasitic resistance is around 320 Ω; (b) The estimated parasitic resistances for different equivalent inductances $L = 3.23$ H, 4.40 H, 6.33 H, 9.89 H, 17.59 H, 39.58 H. It is noted that the parasitic resistance increases with the increase of L.

In the experiment, a harmonic sweep excitation ranging from 200 Hz to 700 Hz is generated with a sweep rate of 2 Hz/sec. **Figure 11** compares the measured transmittances of the graded and uniform piezo-meta-beams shunted to the same synthetic circuits for validating the superiority of the graded design. For the synthetic circuits used in experiments, three different equivalent inductances L, i.e., $L_1 = 23.52$ H, $L_2 = 10.97$ H, $L_3 = 5.64$ H, are considered. The transmittances of the two piezo-meta-beams under the short circuit condition are also provided (dashed curves). The attenuation regions (i.e., transmittance < 0 dB) of the graded and uniform piezo-meta-beam are shaded in pink and blue, respectively. It can be seen that evident valleys are produced, and

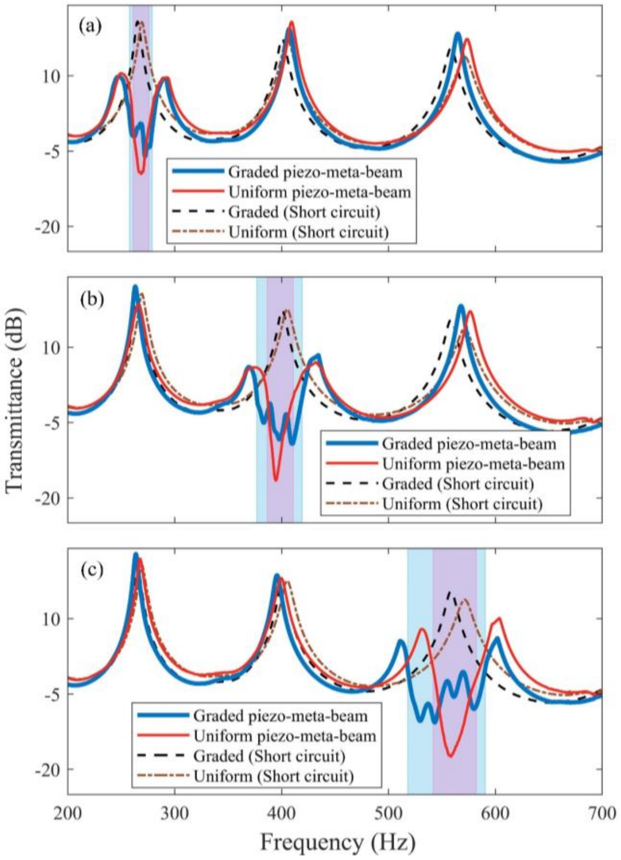

Figure 11. Comparison of the measured transmittances of the graded and uniform piezo-meta-beams with different synthetic inductors: (a) $L_1 = 23.52$ H, (b) $L_2 = 10.97$ H, and (c) $L_3 = 5.64$ H. The measured transmittances when PZT patches are in short circuits are superposed on the plots. The pink and blue shaded areas indicate the vibration attenuation zones of the graded piezo-meta-beam and uniform piezo-meta-beam, respectively.

the modal peaks are significantly suppressed. In general, the graded piezo-meta-beam opens broader attenuation zones than the uniform one, while the attenuation strength is weakened. The attenuation zones of the graded piezo-meta-beams shunted to L_1, L_2, and L_3 are, respectively, 258 Hz - 279 Hz, 377 Hz - 419 Hz, and 518 Hz - 590 Hz. Compared to the attenuation zones in the uniform piezo-meta-beam, i.e., 261 Hz - 276 Hz, 387 Hz - 411 Hz, and 542 Hz - 582 Hz, the bandwidth is enlarged by 40%, 75%, and 80%, respectively. One can also find that it becomes more difficult to broaden the low-frequency attenuation region by using grading PZT patches (e.g., **Figure 11(a)**). Low-frequency vibration suppression and noise reduction are well-known challenging problems. Metamaterials, though with extraordinary properties, also cannot break this law. Many previous studies demonstrated that the ability of conventional uniform metamaterials became evidently weaker in suppressing low-frequency acoustic/elastic waves [53, 54] (i.e., narrower bandgap and weaker attenuation strength). The bandgap of a graded piezoelectric metamaterial is split into discrete attenuation regions due to the “graded” design. Just like conventional metamaterials, the discrete bandgaps are always weaker at low frequencies than at high frequencies. That is why it is more difficult to counteract the mode peaks and expand the attenuation region at low frequencies. Moreover, the multiple resonant peaks of the undamped graded metamaterial system discussed in Section 3.1 disappeared, implying that the wave localization in the non-uniform piezoelectric metamaterial is difficult to achieve due to the inevitable electrical damping in the actual shunt circuits.

Random vibration tests are also carried out to demonstrate the broadband vibration suppression performance of the graded piezo-meta-beam. For brevity, only the case of L_3 = 5.64 H is selected for demonstration. A band-limited white noise excitation is generated with a customized power spectral density (PSD) profile ranging from 480 Hz to 660 Hz, which encompasses a modal peak of the tested beam in short circuit conditions. The PSD is set to be a constant value of 0.001 G^2/Hz, where G is the gravitational acceleration. **Figure 12** compares the PSDs of the graded and uniform piezo-meta-beams measured at the free end, which shows a similar trend to the results in **Figure 11(c)**. **Figure 13(a)** shows the evolution of the root mean square (RMS) accelerations at the beam tips of the two piezo-meta-beams calculated at the free end during 50 seconds of excitation. After a period of time (~10 seconds) for the shaker to reach the predetermined acceleration amplitude, the RMS accelerations at the beam tips remain nearly constant. **Figure 13(a)** shows that the RMS acceleration is reduced from 0.66 G to 0.53 G for the uniform piezo-meta-beam when the piezoelectric shunt circuits are switched on. The improvement in the graded piezo-meta-beam is more significant: the RMS acceleration drops from 0.71 G to 0.38 G. The time-domain acceleration signals at the beam tips of the piezo-meta-beams are plotted in **Figure 13(b)**. The results further confirm that the graded design can offer a better broadband vibration attenuation performance than the uniform counterpart. It is worth mentioning that the theoretical model in Section 2 is phenomenologically and qualitatively, but not quantitatively, validated here. Although the one-dimensional (1D) simplified model of the piezoelectric material has been widely adopted, one defect is yet to be overcome: the predicted bandgap based on the 1D piezoelectric model is always lower than the experimental result. The same problem has been reported in other literature [22, 55]. The possible reason for this is that the internal capacitance of the piezoelectric material is misestimated by the 1D model. Refined modeling of 3D piezoelectric metamaterials and quantitative comparison with experimental results can be a prospective work.

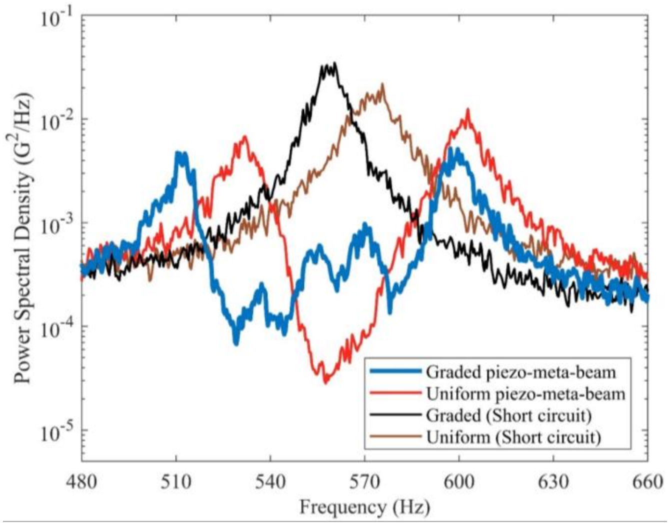

Figure 12. PSDs of the beam tips of the graded and uniform piezo-meta-beams under the band-limited white noise excitation (480 Hz to 660 Hz) with a constant PSD of 0.001 G^2/Hz.

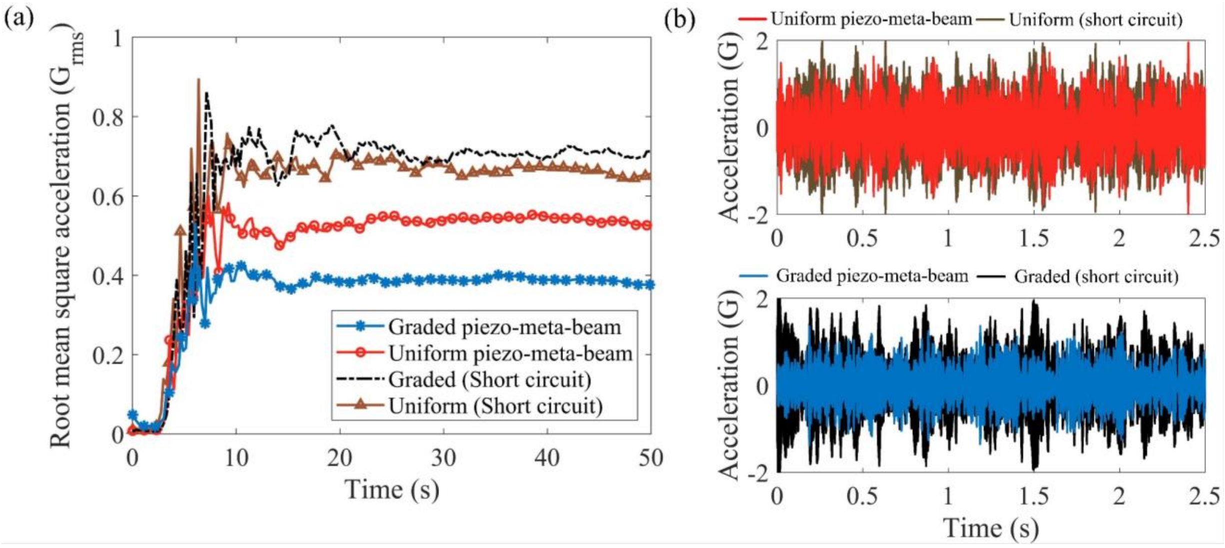

Figure 13. (a) Root mean square (RMS) accelerations at the beam tips of the graded and uniform piezo-meta-beams under the band-limited white noise excitation (480 Hz to 660 Hz) with a constant PSD of 0.001 G^2/Hz. (b) Acceleration signal of the graded and uniform piezo-meta-beams at the tip in the time domain.

5. Conclusions

This paper presented analytical and experimental studies of a metamaterial beam covered by an array of graded piezoelectric transducers for broadband vibration attenuation. We considered a graded supercell and employed the transfer matrix method to solve the dispersion relation. We also derived the transmittance of the graded piezo-meta-beam with a clamped-free boundary condition. Both the band structure and transmittance analysis results indicated that the vibration attenuation zone was widened after introducing length grading on piezoelectric patches but split into pieces by resonant peaks. By leveraging the electrical damping effect, it was shown that the resonant peaks located between those dispersed attenuation zones were damped out, leading to the formation of a continuous attenuation zone for broadband vibration mitigation. However, a parametric study revealed that the bandgap is sensitive to the length grading of the piezoelectric patches. An over-tuned length grading could lead to excessively dispersed attenuation zones and much weakened attenuation capability. Experiments were performed to evaluate the vibration attenuation performance of the graded piezo-meta-beam. The harmonic sweep test confirmed that the attenuation zone generated by the "graded" design could be enlarged by as much as 80%. A random excitation test was also conducted. The results showed that given the power spectral density (PSD) of the random input excitation was 0.001 G^2/Hz, the RMS acceleration amplitude at the tip of the graded piezo-meta-beam could be suppressed to 0.38 G, which was much smaller than 0.52 G of the uniform counterpart.

The proposed graded metamaterial beam is still a laboratory model. Additional tests under various load conditions will be carried out to better understand its limit for practical applications. In addition, one can hopefully further enhance its vibration attenuation capacity by including multiple graded supercells and/or by incorporating more advanced shunt circuits.

Acknowledgments

This work was financially supported by a PhD scholarship from the China Scholarship Council (No. 201907000126).

References

[1] Yi K, Matten G, Ouisse M, Sadoulet-Reboul E, Collet M, Chevallier G. Programmable metamaterials with digital synthetic impedance circuits for vibration control. Smart Materials and Structures. 2020;29:035005.

[2] Jiang W, Yin M, Liao Q, Xie L, Yin G. Three-dimensional single-phase elastic metamaterial for low-frequency and broadband vibration mitigation. International Journal of Mechanical Sciences. 2021;190:106023.

[3] Chen Z, Sun S, Deng L, Yang J, Zhang S, Du H, et al. Investigation of a new metamaterial magnetorheological elastomer isolator with tunable vibration bandgaps. Mechanical Systems and Signal Processing. 2022;170:108806.

[4] Wang Y, Yang J, Chen Z, Gong X, Du H, Zhang S, et al. Investigation of a novel MRE metamaterial sandwich beam with real-time tunable band gap characteristics. Journal of Sound and Vibration. 2022;527:116870.

[5] Bilal OR, Foehr A, Daraio C. Bistable metamaterial for switching and cascading elastic vibrations. Proceedings of the National Academy of Sciences. 2017;114:4603-6.

[6] Ramakrishnan V, Frazier M. Multistable metamaterial on elastic foundation enables tunable morphology for elastic wave control. Journal of Applied Physics. 2020;127:225104.

[7] Fernandes DE, Silveirinha MG. Bistability in mushroom-type metamaterials. Journal of Applied Physics.

2017;122:014303.

[8] Nimmagadda C, Matlack KH. Thermally tunable band gaps in architected metamaterial structures. Journal of Sound and Vibration. 2019;439:29-42.

[9] Li Z, Li Y, Kumar S, Lee HP. Thermal tuning of negative effective mass density in a two-dimensional acoustic metamaterial with hexagonal lattice. Journal of Applied Physics. 2019;126:155102.

[10] Zhao Z, Cui X, Yin Y, Li Y, Li M. Thermal tuning of vibration band gaps in homogenous metamaterial plate. International Journal of Mechanical Sciences. 2022;225:107374.

[11] Han H, Sorokin V, Tang L, Cao D. Lightweight origami isolators with deployable mechanism and quasi-zero-stiffness property. Aerospace Science and Technology. 2022;121:107319.

[12] Fuchi K, Diaz AR, Rothwell EJ, Ouedraogo RO, Tang J. An origami tunable metamaterial. Journal of Applied Physics. 2012;111:084905.

[13] Jiang P, Jiang T, He Q. Origami-based adjustable sound-absorbing metamaterial. Smart Materials and Structures. 2021;30:057002.

[14] Sugino C, Leadenham S, Ruzzene M, Erturk A. On the mechanism of bandgap formation in locally resonant finite elastic metamaterials. Journal of Applied Physics. 2016;120:134501.

[15] Sugino C, Erturk A. Analysis of multifunctional piezoelectric metastructures for low-frequency bandgap formation and energy harvesting. Journal of Physics D: Applied Physics. 2018;51:215103.

[16] Gripp J, Rade D. Vibration and noise control using shunted piezoelectric transducers: A review. Mechanical Systems and Signal Processing. 2018;112:359-83.

[17] Sugino C, Ruzzene M, Erturk A. An analytical framework for locally resonant piezoelectric metamaterial plates. International Journal of Solids and Structures. 2020;182:281-94.

[18] Zheng Y, Tian W, Lee NKX, Qu Y, Meng G. A programmable macro-fiber-composite meta-ring with digital shunting circuits. Journal of Sound and Vibration. 2022:117017.

[19] Alshaqaq M, Sugino C, Erturk A. Programmable Rainbow Trapping and Band-Gap Enhancement via Spatial Group-Velocity Tailoring in Elastic Metamaterials. Physical Review Applied. 2022;17:L021003.

[20] Yi K, Liu Z, Zhu R. Multi-resonant metamaterials based on self-sensing piezoelectric patches and digital circuits for broadband isolation of elastic wave transmission. Smart Materials and Structures. 2021;31:015042.

[21] Airoldi L, Ruzzene M. Design of tunable acoustic metamaterials through periodic arrays of resonant shunted piezos. New Journal of Physics. 2011;13:113010.

[22] Yi K, Collet M. Broadening low-frequency bandgaps in locally resonant piezoelectric metamaterials by negative capacitance. Journal of Sound and Vibration. 2021;493:115837.

[23] Chen Y, Huang G, Sun C. Band gap control in an active elastic metamaterial with negative capacitance piezoelectric shunting. Journal of Vibration and Acoustics. 2014;136.

[24] Alfahmi O, Sugino C, Erturk A. Nonlinear synthetic impedance circuits for piezoelectric structures. Active and Passive Smart Structures and Integrated Systems XVI: SPIE; 2022. p. 123-8.

[25] Zhang X, Yu H, He Z, Huang G, Chen Y, Wang G. A metamaterial beam with inverse nonlinearity for broadband micro-vibration attenuation. Mechanical Systems and Signal Processing. 2021;159:107826.

[26] Bao B, Lallart M, Guyomar D. Structural design of a piezoelectric meta-structure with nonlinear electrical Bi-

link networks for elastic wave control. International Journal of Mechanical Sciences. 2020;181:105730.

[27] Bao B, Lallart M, Guyomar D. Manipulating elastic waves through piezoelectric metamaterial with nonlinear electrical switched Dual-connected topologies. International Journal of Mechanical Sciences. 2020;172:105423.

[28] Li X, Chen Y, Hu G, Huang G. A self-adaptive metamaterial beam with digitally controlled resonators for subwavelength broadband flexural wave attenuation. Smart Materials and Structures. 2018;27:045015.

[29] Fabro AT, Meng H, Chronopoulos D. Uncertainties in the attenuation performance of a multi-frequency metastructure from additive manufacturing. Mechanical Systems and Signal Processing. 2020;138:106557.

[30] Pan W, Tang G, Tang J. Evaluation of uncertainty effects to band gap behavior of circuitry-integrated piezoelectric metamaterial using order-reduced analysis. Journal of Intelligent Material Systems and Structures. 2018;29:2677-92.

[31] Wu X, Li Y, Zuo S. The study of a locally resonant beam with aperiodic mass distribution. Applied Acoustics. 2020;165:107306.

[32] Jian Y, Tang L, Hu G, Wang Y, Aw KC. Adaptive genetic algorithm enabled tailoring of piezoelectric metamaterials for optimal vibration attenuation. Smart Materials and Structures. 2022;31:075026.

[33] Michielsen J, Arteaga IL, Nijmeijer H. LQR-based optimization of multiple tuned resonators for plate sound radiation reduction. Journal of Sound and Vibration. 2016;363:166-80.

[34] Mogilevtsev D, Pinheiro F, Dos Santos R, Cavalcanti S, Oliveira L. Light propagation and Anderson localization in disordered superlattices containing dispersive metamaterials: effects of correlated disorder. Physical Review B. 2011;84:094204.

[35] Thomes RL, Beli D, Junior CDM. Space–time wave localization in electromechanical metamaterial beams with programmable defects. Mechanical Systems and Signal Processing. 2022;167:108550.

[36] Zangeneh-Nejad F, Fleury R. Disorder-induced signal filtering with topological metamaterials. Advanced Materials. 2020;32:2001034.

[37] Gric T, Hess O. Surface waves guided by metamaterials with rotational disorder. Applied Physics A. 2018;124:1-6.

[38] Hu G, Austin AC, Sorokin V, Tang L. Metamaterial beam with graded local resonators for broadband vibration suppression. Mechanical Systems and Signal Processing. 2021;146:106982.

[39] Alshaqaq M, Erturk A. Graded multifunctional piezoelectric metastructures for wideband vibration attenuation and energy harvesting. Smart Materials and Structures. 2020;30:015029.

[40] Liu Y, Han C, Liu D. Broadband vibration suppression of graded/disorder piezoelectric metamaterials. Mechanics of Advanced Materials and Structures. 2022:1-14.

[41] Jian Y, Tang L, Hu G, Li Z, Aw KC. Design of Graded Piezoelectric Metamaterial Beam with Spatial Variation of Electrodes. International Journal of Mechanical Sciences. 2022:107068.

[42] Hagood NW, Von Flotow A. Damping of structural vibrations with piezoelectric materials and passive electrical networks. Journal of sound and vibration. 1991;146:243-68.

[43] Wang G, Cheng J, Chen J, He Y. Multi-resonant piezoelectric shunting induced by digital controllers for subwavelength elastic wave attenuation in smart metamaterial. Smart Materials and Structures. 2017;26:025031.

[44] Yoon H, Youn BD, Kim HS. Kirchhoff plate theory-based electromechanically-coupled analytical model

considering inertia and stiffness effects of a surface-bonded piezoelectric patch. Smart Materials and Structures. 2016;25:025017.

[45] Jian Y, Hu G, Tang L, Xu J, Aw KC. A generic theoretical approach for estimating bandgap bounds of metamaterial beams. Journal of Applied Physics. 2021;130:054501.

[46] Cruz M, Beltrán M, Wang C, Tagüeña-Martínez J, Rubo YG. Supercell approach to the optical properties of porous silicon. Physical Review B. 1999;59:15381.

[47] Yi Q, Zhao C, Wang P. Characteristics of defect states in periodic railway track structure. Journal of Low Frequency Noise, Vibration and Active Control. 2021:14613484211038261.

[48] Wang B, Huang Y, Zhou W, Yang Z. Metamaterial beam for flexural wave resonance rainbow trapping and piezoelectric energy harvesting. Journal of Applied Physics. 2021;129:064505.

[49] De Ponti JM, Iorio L, Riva E, Ardito R, Braghin F, Corigliano A. Selective mode conversion and rainbow trapping via graded elastic waveguides. Physical Review Applied. 2021;16:034028.

[50] Hu G, Lan C, Tang L, Yang Y. Deep-subwavelength interface states in mechanical systems. Mechanical Systems and Signal Processing. 2022;169:108598.

[51] Wang G, Chen S, Wen J. Low-frequency locally resonant band gaps induced by arrays of resonant shunts with Antoniou’s circuit: experimental investigation on beams. Smart Materials and Structures. 2010;20:015026.

[52] Tang J, Wang K-W. Active-passive hybrid piezoelectric networks for vibration control: comparisons and improvement. Smart Materials and Structures. 2001;10:794.

[53] El-Borgi S, Fernandes R, Rajendran P, Yazbeck R, Boyd J, Lagoudas D. Multiple bandgap formation in a locally resonant linear metamaterial beam: Theory and experiments. Journal of Sound and Vibration. 2020;488:115647.

[54] Wang K, Zhou J, Tan D, Li Z, Lin Q, Xu D. A brief review of metamaterials for opening low-frequency band gaps. Applied Mathematics and Mechanics. 2022;43:1125-44.

[55] Silva TMP, Clementino MA, de Sousa VC, De Marqui C. An experimental study of a piezoelectric metastructure with adaptive resonant shunt circuits. IEEE/ASME Transactions on Mechatronics. 2020;25:1076-83.